The influence of soil fabric on the monotonic and cyclic shear behaviour of consolidated and compacted specimens

Isabella Novais Silva

BEng (Hons)

PhD Candidate, Transport Research Centre, University of Technology Sydney, NSW 2007. Australia.

ORCID ID: https://orcid.org/0000-0003-3318-6772

Buddhima Indraratna[1]

PhD (Alberta), MSc (Lond.), BSc (Hons., Lond.), DIC, FTSE, FIEAust., FGS, CEng, CPEng

Distinguished Professor of Civil Engineering, Founding Director of Australian Research Council's Industrial Transformation Training Centre for Advanced Technologies in Rail Track Infrastructure (ITTC-Rail), Director of Transport Research Centre, School of Civil and Environmental Engineering, University of Technology Sydney, NSW 2007, Australia.

ORCID ID: https://orcid.org/0000-0002-9057-1514

[1]Corresponding author e-mail: buddhima.indraratna@uts.edu.au

Thanh T. Nguyen

PhD

ARC-DECRA Fellow, Transport Research Centre, School of Civil and Environmental Engineering, University of Technology Sydney, NSW 2007, Australia.

ORCID ID: https://orcid.org/0000-0001-6078-2559

Cholachat Rujikiatkamjorn

PhD, MEng (AIT), BEng (Hons)

Professor, Transport Research Centre, School of Civil and Environmental Engineering, University of Technology Sydney, NSW 2007, Australia.

ORCID ID: https://orcid.org/0000-0001-8625-2839

Figures: 14

Tables: 2

Submitted to: Canadian Geotechnical Journal

Abstract

While the fabric of soil can significantly influence its behaviour, the effect of varying fabric parameters on the subgrade shear response is still not well understood. This study creates soil specimens with different fabrics which are then captured through X-ray microscopic-computed tomography scanning (micro-CT) and quantified by image processing techniques. A comprehensive laboratory investigation is conducted to understand how the soil fabric affects its monotonic and cyclic shear behaviour. The results indicate that the consolidation method creates a more homogeneous fabric with mainly small to medium interconnected pores, whereas the compaction technique creates significantly large and mostly inter-aggregate pores with lower connectivity. In this regard, the consolidated specimens exhibit an elastic-perfectly plastic behaviour, while the compacted specimens show strain-hardening transformation during isotropic monotonic shearing. Under anisotropic conditions, the compacted specimens exhibit a greater strain softening response and excess pore pressure than the consolidated specimens because they have a weaker fabric. Furthermore, the compacted specimens show a smaller threshold strain at a lower critical number of cycles due to the collapse of large pores. These current findings prove the decisive role that soil fabric plays in determining the shear response and failure of subgrade soils.

Keywords

Soil fabric, micro-CT scanning, shear behaviour, railway subgrade, cyclic loading

1 Introduction

Soil fabric refers to the geometrical assembly of particles and groups of particles and pores, while microstructure incorporates the soil fabric apart from the particle composition and interparticle forces within a soil matrix (Mitchell and Soga 2005). The development of soil microstructure in nature is influenced by the formation and stress history of the soil (Jana and Stuedlein 2021), certain chemical processes such as cementation (Burghignoli *et al.* 2010), and physical processes such as wetting and drying cycles (Burton *et al.* 2015). Microstructure can have a significant effect on the permeability, compressibility, shear strength, and stiffness of the soil (Burland 1990; Pillai *et al.* 2011; Jung *et al.* 2012). The well-known stress anisotropy concept (i.e., the ratio between effective horizontal and vertical stresses) is often used to relate the soil fabric to its stress-strain responses (Cai *et al.* 2018; Silva *et al.* 2022). For instance, Hyodo *et al.* (1994) and Silva *et al.* (2022) showed that clayey soils subjected to higher levels of stress anisotropy can exhibit increased shear strength. Besides that, the role of microstructure on the shear behaviour of undisturbed and remoulded specimens is widely recognised (Leroueil and Vaughan 1990; Liu and Carter 2002; Gasparre *et al.* 2007).

Over the past couple of decades, the relationship between the micro and macro characteristics of soil has received a great deal of attention (Li and Li 2009; Romero 2013; Ge *et al.* 2021), partly due to a rapid advancement in the use of micro-examination techniques to establish salient features at the soil micro-scale domain (i.e., a few microns). Micro-CT scanning is an advanced non-destructive technique that allows 2D and 3D micro-characteristics of a porous specimen to be quantified; thus making this approach increasingly popular (Cnudde and Boone 2013; Fonseca *et al.* 2013c; Taylor *et al.* 2015). For example, Fonseca *et al.* (2013c) used micro-CT scanning to quantify the fabric of specimens of sandy soil under triaxial compression at various levels of shear strain, while Cnudde *et al.* (2011) estimated the porosity and sphericity of grains using a 3D reconstruction of micro-CT images. Despite considerable success, past studies have mainly concentrated on coarse particles and pores of sands and rocks, while limited effort has been made to investigate fine-grained soils.

In Australia, most rail systems have been built along the coastal line over low-lying regions of soft soil deposits; hence, ground modification techniques, including consolidation and compaction methods are commonly applied to improve the ground conditions (Chu *et al.* 2014; Indraratna *et al.* 2018). They can alter the microstructure of the natural subsoil and induce the formation of new soil fabrics. In the laboratory the influence of fabric on soil behaviour can be assessed using various techniques of specimen preparation. For instance, Pillai *et al.* (2011) found that a clayey soil with a dispersed structure exhibited higher peak stress followed by strain softening, while flocculated soils showed a strain hardening behaviour. On the other hand, Vaid and Sivathayalan (2000) explained that sandy specimens prepared by moist tamping had less shear strength and were more prone to static liquefaction than test specimens reconstituted by water pluviation. Although these studies qualitatively assessed the effect of fabric on monotonic shear behaviour, they did not quantify fabric parameters of soil specimens to capture intrinsic relationships between the soil fabric and the corresponding macroscopic (conventional) response.

Although several studies have shown that the cyclic shear response of soils is influenced by their fabric, our understanding is still limited, especially compared to the monotonic shear behaviour. Most previous experiments (Sze and Yang 2014; Wichtmann *et al.* 2020; Jana and Stuedlein 2021) focused on the influence of specimen preparation methods on the cyclic shear behaviour of sandy soils subjected to low frequencies (i.e., $f \leq 1$ Hz), whereas the influences of high frequency and cyclic stress ratios more appropriate for heavy-haul railways have not been investigated extensively. For example, Wichtmann *et al.* (2020) carried out cyclic triaxial tests ($f = 0.2$ Hz) on a sandy soil reconstituted by several preparatory methods and found that the development of axial strain was significantly influenced by the soil fabric, especially in the medium-dense specimens. Similarly, Sze and Yang (2014), through a series of undrained cyclic tests ($f = 0.01$ Hz), showed that specimens prepared by moist tamping developed higher cyclic resistance than those prepared by dry deposition. Nevertheless, none of these studies could quantify the microstructural features and their impact on the cyclic response of soil, and although considerable effort has gone into characterising the relationship between monotonic and cyclic shear failures, the influence of the soil fabric on this complex issue has still not been addressed. Some previous studies found that the monotonic shear response of soil is pertinent because it sets a common boundary with cyclic failure (Georgiannou *et al.* 1991; Yang and Pan 2017), whereas other studies revealed that the cyclic stress paths can cross the strength envelope or the critical state line (CSL) obtained from static tests (Sakai *et al.* 2003; Dzaklo *et al.* 2021). While there seems to be a lack of attention paid to the role of soil fabric in these controversial findings, an insightful investigation focused on the mechanisms through which distinct micro-porous structures can affect both monotonic and cyclic shear failures would be invaluable.

In view of the above, this study aims to advance our understanding of how fabric features of subgrade soils subjected to consolidation or compaction can influence their properties, and their monotonic and cyclic shear behaviour. In this regard, a subgrade soil (clayey sand) was collected from a railway site in NSW, Australia where track degradation has been regularly reported. The samples were reconstituted either by slurry consolidation or compaction methods to create specimens resembling typical subgrade formations. Conventional static and cyclic triaxial tests were carried out to understand the fundamental properties of the soil, the stress-strain responses, and the failure mechanisms. Micro-CT scanning coupled with image processing techniques was used to help quantify the fabric parameters of the specimens and clarify their distinct shear responses.

2 Laboratory investigation

2.1 Soil properties

Samples of subgrade soil were collected from depths of 0.5-1.0 m from a rail track in the South Coast line (south of Sydney), Australia that was experiencing a high degree of fouling. A series of laboratory tests were carried out to investigate the basic soil properties, they included the Atterberg limits (ASTM D4318-17e1 2017), specific gravity (ASTM D854-14 2014), particle size distribution, and standard proctor compaction test (ASTM D698-12e2 2012). The soil had a liquid limit, LL = 38 and a plastic limit, PL = 18, thus plasticity index PI = 20, with a specific gravity of 2.71. The particle size distribution was determined by sieve analysis (ASTM C136/C136M-19 2019) and laser diffraction. The results indicated a gap-graded soil with 58%, 15% and 27% of sand, silt and clay, respectively. The soil could be classified as clayey sand of low-moderate plasticity (*i.e.*, SC) according to the Unified Soil Classification System (ASTM D2487-17e1 2017). The maximum dry density (MDD) and optimum moisture content (OMC) were 18.2 kN/m^3 and 12.8%, respectively.

2.2 Soil specimen preparation

Two different preparation methods were used to replicate subgrade specimens subjected to consolidation and compaction techniques, which are commonly adopted in railways. The consolidation method simulates the subgrade consolidation under an embankment loading and/or a natural deposition process. On the other hand, the compaction method was used to reproduce a subgrade soil formed by compaction in the field to establish a suitable subgrade foundation. Consolidation typically requires significantly more time compared to soil compaction. For instance, the consolidation of a soft soil beneath an embankment can take over 18 months (Indraratna *et al.* 2018), resulting in a distinctly different soil fabric compared to a rapid (dynamic) compaction process.

In the slurry consolidation method the soil sample was dried and mixed with distilled and de-aired water with a moisture content of 1.2 times the *LL* (i.e., w = 45.6%). The slurry was transferred into 50 mm in diameter by 180 mm one dimensional consolidation cells. The specimens were then subjected to incremental loading stages up to a vertical stress of 50 kPa, which is within the in-situ stress range for shallow subgrades beneath railways (Indraratna *et al.* 2020a). The extruded specimens were then carefully trimmed to a height of 100mm. The density and void ratio of the specimens were calculated based on their water content, total weight, and volume. The average void ratio (e_o) and dry density (γ_d) were 0.66 and 16 kN/m^3, respectively. Specimens representing a compacted subgrade foundation were first dried, mixed with distilled water at a moisture content of 11.5%, and kept in a humidity-controlled chamber for 24h before being compacted. It is noteworthy that the moisture content adopted in the specimen preparation corresponds to the in-situ water content measured during the sample collection. The compaction was carried out using a split mold (50 mm diameter by 150 mm height) and a compaction hammer with a mass of 528 g and a drop height of 182 mm. The specimens were compacted in 10 layers of 10 mm height to ensure uniformity. Each layer received 6 blows and had its surface scarified before the next layer was compacted to ensure the continuity of the layers. The soil mass required for each layer was calculated to achieve the target void ratio and dry density, which were the same as the consolidated specimens. The dry density of 16 kN/m^3 corresponds to a relative compaction of approximately 90%. Figure 1 shows consolidated and compacted samples before triaxial testing. Visual observations indicate a significant difference between their fabric, i.e., the compacted specimen looks more porous compared to the consolidated one.

2.3 Assessment of soil fabric

2.3.1 Micro-CT scanning of soil specimens

The micro-CT scanner can achieve very high nominal resolutions (< 4 µm) and was fully automated with a high-speed X-ray source (20 – 100 kV, 10W) and an X-ray detector (active pixel CMOS flat-panel, 3MP – 1944 x 1536 pixels). During scanning, X-rays at 80 kV and 125 µA were emitted and passed through the specimen before being received by the X-ray detector. The specimens followed a circular trajectory (360°) at increments of 0.4°. After each increment, 5 frames were captured and averaged to ensure a high-quality 3D reconstruction of the specimens' fabric. In micro-CT scanning, the intensity of the X-rays is attenuated as they pass through specimens, depending on their density, including the particles and voids. The attenuated values are received by the X-ray detector and result in greyscale projections that represent the distribution of X-ray intensity throughout the specimen; they are subsequently used to reconstruct a 3D image of the soil fabric (Nguyen *et al.* 2019). It is noteworthy that beam hardening and ring artifacts can compromise the quality of the image reconstruction and the subsequent analysis (Cnudde and Boone 2013; Wildenschild and Sheppard 2013). To mitigate this problem and improve the accuracy of the images, a 1-mm thick aluminium (Al) filter was placed between the source of the X-ray and the specimens, as recommended by previous studies (Ren *et al.* 2016; Nguyen and Indraratna 2019).

During micro-CT scanning, the specimens are positioned close to the source of the X-ray and are contained within the field of view of the X-ray detector, this means the space resolution of the output image can then be related to the dimensions of the specimen (Cnudde *et al.* 2011). In this study, the specimens (approximately 20 mm in diameter by 30 mm high) used for CT scanning were cored from the oven-dried triaxial specimens. Their size was selected according to the desired space resolution and the scale of soil particles to ensure a representative specimen. The focal length was adjusted automatically, thus attaining optimum voxel sizes of 11.2 μm and 12.7 μm for the consolidated and compacted specimens, respectively. In comparison with the size of the grains in these soil specimens, the voxel sizes are approximately 6 to 7 times smaller than 0.075 mm, which represents the boundary between fine (i.e., silt and clay particles) and coarse (sand) grains. As a result, the fine grains generally appear as a cluster of particles in the output images, although some coarse grains may still be identified individually. It is worth mentioning that the arrangement of the soil particles is an important aspect of the soil fabric which has received a lot of attention in the past (Sivakumar *et al.* 2002; Yimsiri and Soga 2011; Fonseca *et al.* 2013b; Chen *et al.* 2020), while the characterisation of the pore space has been limited. Therefore, this study focuses on quantifying specific features of the pore space while general aspects of the solid space are discussed.

2.3.2 Image processing and analysis of micro-CT images

The radiographs were reconstructed in the software NRecon v1.7.0 (SkyScan NV 2011), resulting in a series of greyscale 2D cross-sections at each 1 voxel height of the specimens. In the output images, the bright areas represent a higher level of X-ray attenuation, hence the soil particles had lighter shades of greyscale i.e., higher values of intensity, than the void spaces. Image processing and analysis took place on MATLAB (MathWorks 2019) using built-in functions. First, an 800 x 800- pixel region of interest (ROI) was selected from the output images, and then image processing techniques such as pre-processing, binarization, pore segmentation and post-processing were applied. During pre-processing, contrast adjustment and filtering techniques were applied to improve the quality of the images and, ultimately, the accuracy of the segmentation results. A median filter was used to reduce the noise, i.e. fluctuations in voxel intensity, that usually appears in the output images due to signal disturbances during scanning and inaccuracies during the reconstruction process (Taylor *et al.* 2015; Gonzalez and Woods 2018).

Subsequently, a binarization process was utilised to label the soil particles and void space according to the thresholding method proposed by Otsu (1979). The morphological watershed method was then used to segment the pore space into individual voids in order to quantify the specimens' microfeatures (Shi and Yan 2015; Rabbani *et al.* 2016). Post-processing was carried out after binarization and segmentation to calibrate the results and ensure that the image analysis detected actual pores rather than noises that could have persisted after pre-processing or which appeared after segmentation. In this step, a morphological operation was applied to remove pores that were less than 2 pixels.

2.4 Triaxial test program

A total of 16 monotonic and 16 cyclic undrained triaxial tests were carried out on isotropically and anisotropically consolidated specimens; the relevant details are given in Tables 1 and 2. These experimental procedures took place in the following 4 stages, i.e., (1) flushing, (2) saturation, (3) consolidation, and (4) shearing (summarised in Figure 2):

- Stage (1): The specimens were flushed under an effective confining pressure of 5kPa until a constant flow rate was attained and no air bubbles were observed.
- Stage (2): Saturation was carried out by increasing the back pressure at a rate of 0.35 kPa/min up to 500 kPa, where it remained constant until the value of Skempton's coefficient (B) > 0.95 was reached.
- Stage (3): The specimens were isotropically and anisotropically consolidated. During isotropic consolidation, five levels of confining pressure ranging from 50 kPa to 300 kPa were applied. It is of interest to realise that the vertical stresses in subgrades under railways due to heavy-haul axle loads can exceed 300 kPa (Indraratna *et al.* 2010). Therefore, the maximum confining pressure for testing was adopted based on practical considerations. During anisotropic consolidation, the stress path was controlled to reach the target ratio between effective horizontal and vertical stresses (i.e., $K = \sigma'_3/\sigma'_1$) in the $p' - q$ plane, where $p' = (\sigma'_1 + 2\sigma'_3)/3$ and $q = \sigma'_1 - \sigma'_3$. The target K values for the monotonic triaxial shearing varied from 0.5 to 0.94, this conforms

with the in-situ condition of normally consolidated soils found in low-lying regions of Eastern NSW (Pineda *et al.* 2016; Silva *et al.* 2022). The value of K = 0.5 corresponds to the at-rest earth pressure coefficient (i.e., K_0) determined by Silva *et al.* (2022). Therefore, anisotropic consolidation was carried out up to $p'_0 \cong$ 34 kPa, which is in conformity with the in-situ range for shallow subgrades beneath railways (Liu and Xiao 2010; Indraratna *et al.* 2020a) and coincides with the maximum stresses applied to the consolidated specimens during the specimen preparation (i.e., σ'_1 = 50 kPa and K_0 = 0.5, hence $p' \cong$ 34 kPa). For cyclic triaxial shearing, all the specimens were anisotropically consolidated up to $p'_0 \cong$ 34 kPa and K_0 = 0.5.

- Stage (4): The monotonic and cyclic shearing were conducted in fully undrained conditions, i.e. no volumetric strains were developed during this stage. During monotonic loading, the specimens were sheared at a strain rate of 0.01 mm/min up to an axial strain (ε_a) of 20%. In cyclic shearing, a stress-controlled one-way loading with a sinusoidal waveform was used to simulate the stress generated in the subgrade soil by a moving train (Lei *et al.* 2016; Indraratna *et al.* 2020b). In this study, the magnitude of the cyclic stress was represented by the cyclic stress ratio (CSR), which is the ratio of the cyclic deviator stress (Δq) over twice the effective confining pressure (σ'_3).

Two CSRs, i.e., 0.2 and 0.3, were applied to simulate moderate levels of cyclic stress, with Δq varying from 10 kPa to 15 kPa. In-situ measurements reported by Liu and Xiao (2010) showed that this range corresponds to the stresses generated at 0.5m – 1m below the subgrade surface by a passenger train with 14-tonne axle load travelling at 200 km/h or a freight train with 23-tonne axle load travelling at 120 km/h. The cyclic deviator stress was applied at loading frequencies varying from 1Hz to 5Hz, to represent the attenuated frequency generated by trains travelling at speeds from 50 km/h to 200 km/h (Priest *et al.* 2010; Trinh *et al.* 2012; Mamou *et al.* 2017; Li *et al.* 2018; Zhao *et al.* 2021).

3 Results and Discussion

3.1 Analysis of soil fabric

In the analysis of micro-CT images, 1128 cross-sections were assessed along 14.36 mm and 12.64 mm height of the compacted and consolidated specimens, respectively (i.e, one cross-section at 0.011-0.013 mm intervals). It is important to mention that no boundary discontinuity between layers were observed in the micro-CT scans of the compacted specimen. Figure 3 shows the image processing in the ROIs of representative cross sections. The binary ROIs (Figures 3c and 3d) indicate pixels with values of either 0 (black), representing the pore regions, or 1 (white), representing clusters of fine and coarse soil particles, i.e., the solid regions. Figure 3 also shows that the consolidated specimen had a more homogeneous fabric with uniformly distributed small pores, while the compacted specimen had large clusters of soil aggregates and large continuous pores, which confirms the initial visual observations (Figure 1).

The porosity (n) was calculated after binarization as the number of pixels in the pore space $\left(N_{pixel}^{pore}\right)$ over the total number of pixels in the ROI $\left(N_{pixel}^{total}\right)$, therefore:

$$n = \frac{N_{pixel}^{pore}}{N_{pixel}^{total}} \quad (1)$$

The n values were 0.33 and 0.29 for the compacted and consolidated specimens, respectively. Compared to the measured porosity of 0.39, the results from the image processing were underestimated by 15% and 25%; this range is similar to that measured by Fonseca *et al.* (2013c). This limitation was caused by the resolution of the micro-CT scans that could not capture micropores smaller than 12.7 μm and 11.2 μm for compacted and consolidated specimens, respectively. Nevertheless, the images showed considerable differences in the macropores; they were then quantified and are shown in Figure 4. The pore size distribution in terms of equivalent pore diameter (Figure 4a) confirms that the consolidation method creates pores that are much smaller than the compaction method. For example, 60% of the pores in the consolidated specimen had a diameter smaller than 67.4 μm (i.e., d_{60} = 67.4 μm), while the diameter of the compacted specimen was almost double at the same percentage (d_{60} = 129 μm). To investigate the shape of the pores, the lengths of the minor and major axes of the ellipses that encompass individual pores were estimated, as shown in Figure 4b. It is interesting that the lengths of the major axes of the pores created by compaction were much larger than those created by consolidation. The distribution of the minor axis length of the compacted specimens was almost the same as the major axis length of the consolidated specimen. The circularity (roundness) of pores with Area > 100 pixels was also calculated. The circularity (C) is determined by $4 \cdot Area \cdot \pi / Perimeter^2$, where C = 1 represents a perfect circle. The results shown in Figure 4c indicate that the pores in the consolidated specimen are not as round as those in the compacted specimen; for example, in the consolidated specimen $C_{50} = 0.33$, whereas in the compacted specimen $C_{50} = 0.43$; here the subscript 50 denotes the percentage of pores at 50%. This result probably occurred because the compacted specimens had much larger clusters of aggregated particles, which resulted in larger intra-aggregate pores (Figure 4a), and therefore the influence of individual particle shape on the porous structure was not as significant.

The reconstruction of a volume of interest (VOI) in the middle portion of the specimens was performed on MATLAB (MathWorks 2019) by combining 400 adjacent reduced half-ROIs (i.e., total volume = 400^3 voxels). Image processing and analysis of the 3D VOI followed the same procedure as the 2D ROI. Figures 5a and 5b show the reconstructed solid and pore spaces where the pores (blue areas) are much larger in the compacted specimens. In order to calculate the specific surface area (*S*), the pore space was extracted from the VOI, as shown in Figures 5c and 5d. The specific surface area *S* can be defined as the ratio of the surface area of pores to the total volume of the VOI (Hussaini and Dvorkin 2021). *S* is an important fabric parameter that relates to the fluid conductivity of a porous media. For example, the Kozeny-Carman equation defines permeability as a function of *S*, *n,* and the tortuosity of the pore space (τ) (Mavko *et al.* 2009). The estimated *S* values for the consolidated and compacted specimens were 11.7 mm^{-1} and 6.5 mm^{-1}, respectively. This implies that the consolidated soil would have a larger surface contact area, resulting in lower hydraulic conductivity.

After the pore spaces had been extracted and segmented, 3D pore networks were generated by following the algorithm proposed by Rabbani *et al.* (2014). In this algorithm, the pores are assumed as spheres and the pore throats as cylinders which connect to form the pore network. Figure 6 shows the pore networks of the consolidated and compacted specimens. The pore centres are represented by spheres of different sizes and colours to represent the difference between the pore sizes (diameter), while the pore throats are represented by different colours depending on their length. It is interesting that the consolidated specimen had a higher number of pores per volume than the compacted specimen, while the latter had larger pore diameters and throat sizes, despite having the same density as the former (and thus overall porosity). In summary, the analysis of the pore network revealed that the consolidated specimen had mainly small to medium interconnected pores which were well connected and distributed in a relatively uniform manner, whereas the compacted specimens had much larger pores with lower connectivity. In the consolidation method, the slurry with a uniform mixture of soil particles and water (at high water content, i.e., w = 45.6%) was consolidated to gradually expel the water out of the specimen via dissipation of excess pore water pressure. This relatively slow process coupled with the uniform state of the slurry resulted in more homogeneous and smaller pores. In the compaction method, the unsaturated soil specimens had a considerably smaller water content (i.e., w ≅ 11.6%). These specimens containing a relatively large number of particle clusters were densified by drop shocks, leading to even larger clusters of soil particles, hence larger pores in the altered soil fabric. The next sections will explain how these different porous structures can affect soil behaviour.

3.2 Compressibility and permeability

Oedometer tests were carried out as per ASTM D2435/D2435M-11 (2020) to evaluate the compressibility of the soil, as shown in Figure 7a. The dash line represents the measurements taken as the slurry consolidated. The effective vertical pre-consolidation stresses (σ'_{vc}) determined using the Casagrande method were 35 kPa and 18 kPa for the consolidated and compacted specimens, respectively; note that these specimens had similar initial dry densities. It is interesting to find that the deformation that took place in the compacted specimen shortly after σ'_{vc} was greater than the consolidated specimen; this could be due to the collapse of the large intra-aggregate pores (Figure 3). Previous studies showed there might be greater compressibility after σ'_{vc} as the initial soil structure alters, particularly for compacted soils (Ge *et al.* 2021). When σ'_v > 100 kPa, the compressibility curves were almost parallel to each other with compression indices (C_c) of 0.19 and 0.18 for consolidated and compacted specimens, respectively. The swelling indices (C_s) were approximately 0.019, i.e., 10% of C_c.

Figure 7b shows the variation of the coefficient of consolidation (c_v) with the average effective vertical stress ($\overline{\sigma}'_v$) between two load increments. It is noticeable that c_v had higher values until σ'_{vc} was reached, which may be due to the alteration of the initial soil fabric, then it remained relatively constant at 5.5 m^2/year and 115.2 m^2/year for the consolidated and compacted specimens, respectively. This remarkable difference in c_v of nearly 2 orders of magnitude reflects the effect of fabric because since the compacted specimen presented an open fabric with larger intra-aggregate pores it was expected to have higher permeability and faster consolidation. This can be supported using the back calculated coefficient of permeability (*k*) and permeability tests carried out in the triaxial cell with $\sigma'_3 \cong 10$ kPa and hydraulic gradients (*i*) of 5 and 10 for compacted and consolidated specimens, respectively. Figure 7c shows that the permeability in the logarithmic scale decreases almost linearly with the void ratio, and the estimated value of *k* is close to the measured values (open symbols) for $e \cong 0.67$. Similar to c_v, the permeability of the compacted specimens was approximately 2 orders of magnitude higher than the consolidated specimens.

3.3 Monotonic shear behaviour

3.3.1 Isotropic response

As Figure 8a shows, the 3D critical state bounding surface for compacted specimens is confined within the surface delimited by those prepared by consolidation. The critical state was defined as the state at which the soil continued to deform at an approximately constant stress ratio (q/p') and excess pore water pressure. The projections on the $p' - q$ plane (Figure 8b) show the effective stress paths for specimens isotropically consolidated at different levels of p'_0 and the slope of the critical state lines for consolidated and compacted specimens (M_{cons} = 1.38 and M_{comp} = 1.41). Although the stress paths for each test series followed a unique trajectory, they seemed to reach approximately the same critical state line (CSL), which was expected because the specimens had almost the same friction angles (φ_{cons} = 34.1° and φ_{comp} = 34.9°). This suggests the quasi-unique characteristics of CSL regardless of which method is used to prepare the specimens, i.e., the initial fabric. While previous studies generally concur that the soil fabric has little influence on the CSL in the $p' - q$ space (Liu and Carter 2002; Sivakumar *et al.* 2002; Pillai *et al.* 2011), contradicting results were also observed on p' (log scale) – specific volume (v) plane, (Jotisankasa *et al.* 2009; Tarantino 2011; Fonseca *et al.* 2013a). Figure 8c shows that the position of the CSL is affected by the soil fabric on the p' (log scale) – v plane. Even though the slope was approximately the same (λ = 0.075), the CSL for consolidated specimens was above the CSL for compacted specimens with the specific volume at p' = 1 kPa, being Γ_{cons} = 1.808 and Γ_{comp} = 1.760. Similarly, the normally consolidated lines (NCL) obtained from the isotropic compression were parallel with λ = 0.075, but the specific volume at p' = 1 kPa were N_{cons} = 1.887 and N_{comp} = 1.845. The reason for this could be attributed to the collapse of large intra-aggregate pores in the compacted specimen upon reaching the pre-consolidation stress, resulting in the sharp reduction in the void ratio shown in the compressibility curve (Figure 7).

Figure 9a shows the stress-strain responses of the specimens during isotropic shearing. All the specimens seem to reach the peak shear strength at a relatively small axial strain, which agrees with previous studies on clayey sands or sand-clay mixtures (Prakasha and Chandrasekaran 2005; Bayat *et al.* 2014; Cabalar and Mustafa 2017). This is because soils with a high sand content are usually less ductile and the peak shear strength is achieved at a smaller axial strain compared to clayey soils. The consolidated specimens generally exhibited an elasto-perfectly plastic behaviour, while the compacted ones showed a local peak deviator stress (q_{max}) followed by strain softening, a quasi-steady region and finally strain hardening. This transition from strain softening to strain hardening marks a phase transformation state where the soil behaviour shifts from a contractive to a dilative response. It is noteworthy that the strain hardening was more pronounced for compacted specimens at higher levels of p'_0, probably because fabric distortion was greater during shearing at lower confining pressures. At higher confining pressures, the soil fabric had higher resistance to shearing. At the same time, the stresses transferred (arching) mainly to the stronger and more intact parts of the structure, ultimately leading to an increase in the shear stress (strain hardening). Similar partially contractive behaviour was observed for silty and medium-dense sandy soils (Hyde *et al.* 2006; Georgiannou *et al.* 2018). It is also interesting to note that the compacted specimens exhibited a higher q_{max} than those prepared by consolidation, regardless of the level of p'_0, and despite the difference increasing with a higher p'_0. For example, for p'_0 = 50 kPa, $q_{max\ (cons)}$ = 29.4 kPa and $q_{max\ (comp)}$ = 31.1 kPa, while for p'_0 = 300 kPa, $q_{max\ (cons)}$ = 152.9 kPa and $q_{max\ (comp)}$ = 167.5 kPa. In terms of the development of excess pore water pressure (*EPWP*), Figure 9b shows that ultimately, similar levels of *EPWP* were reached while shearing the test specimens consolidated to the same level of p'_0. For example, for p'_0 = 100 kPa, the *EPWP* at the CSL were 80.5 kPa and 82.1 kPa for consolidated and compacted specimens, respectively. As a result, the shift between the NCL and CSL in the $p' - v$ space (i.e., $\mathrm{N} - \Gamma$) was similar (Figure 8b), and the stress paths reached the same CSL in the $p' - q$ space (Figure 8c), even though the specimens were prepared using different techniques.

3.3.2 Anisotropic response

The stress paths for anisotropically consolidated specimens with an initial mean effective stress $p'_0 \cong$ 34 kPa and K varying from 0.50 to 0.94 are shown in Figure 10a. As K decreased (higher anisotropy), the specimens exhibited higher peak deviator stresses and increased brittleness during shearing. While the effect of stress anisotropy on the shear response of soil was similar to that reported in previous studies (Hyodo *et al.* 1994; Yang and Pan 2017; Cai *et al.* 2018; Silva *et al.* 2022), the influence of soil fabric on such a relationship has not been addressed insightfully. Specifically, Figure 10b shows that the strain softening behaviour is more prominent in the compacted specimens regardless of the K ratio, which means that after attaining $q_{max,}$ the specimens showed more significant contraction than those prepared by the consolidation method. As a result, the ratio of $EPWP/p'_0$ was much greater in the compacted specimens (Figure 10c). For instance, for specimens consolidated under K = 0.94, the $EPWP/p'_0$ ratios at the residual shear strength (q_{res} – equivalent to the shear strength at the critical state) were ≅ 0.93 and 0.75 for compacted and consolidated specimens, respectively. This observation confirmed that the open and heterogeneous soil fabric created by the compaction method was more sensitive to the fabric distortions that occurred during shearing at a low level of p'_0.

Figure 10d shows that the shear strength q_{max} for various K ratios was not significantly affected by the preparation method, provided the specimens were consolidated to the same K ratio before shearing. This result corroborated the earlier findings in the isotropic condition (Figure 8) where there was only a marginal difference in q_{max} between the consolidated and compacted specimens at low p'_0 (e.g., 50 kPa). However, there was a much greater impact in q_{res}, probably because the larger shear strains (> 5%) contributed to larger fabric distortion. Figure 10d shows that q_{res} for compacted specimens was much lower, irrespective of the K ratio. For example, for K = 0.5 q_{max} was ≅ 35 kPa for both specimens, but q_{res} were ≅ 26 kPa and 20 kPa for the consolidated and compacted specimens, respectively. It is important to note that the shear behaviour of compacted soil specimens subjected to a low p'_0 was similar to the flow-deformation type of response usually observed for loose sand, indicating a significant post-peak reduction in shear strength (Sze and Yang 2014; Pan *et al.* 2018). This was probably because the large pore spaces in the compacted specimens resulted in a more unstable fabric that was prone to more significant rearrangement during shearing at low confining pressures.

The above sections have demonstrated the influence of soil fabric on the monotonic shear behaviour of consolidated and compacted specimens. In the following section, the authors will discuss how the specimens can behave differently when subjected to cyclic loading. The relationship between the monotonic and cyclic responses will be addressed while considering the effect of the soil fabric in specimens anisotropically consolidated up to p'_0≅ 34 kPa and K_0 = 0.5.

3.4 Cyclic shear behaviour

Figure 11 shows the development of ε_a and $EPWP/p'_0$ with the number of cycles where the results are plotted up to ε_a = 10% for clarity. The cyclic response seemed consistent through a range of CSR and *f* regardless of the fabric and all the specimens failed due to cyclic softening. The critical number of cycles (N_c) and the corresponding threshold axial strain (ε_t) determines the limit above which significant permanent deformation and *EPWP* development occurs. The N_c and ε_t define where the soil behaviour becomes overly non-linear (predominantly plastic response) and the axial strain increases rapidly. As the CSR increased from 0.2 to 0.3, the specimens failed under a smaller number of cycles (i.e., lower N_c). For a given CSR, the specimens failed at a larger number of cycles (i.e., higher N_c) as the frequency increased from 1 Hz to 5 Hz. This occurred because higher loading magnitudes (i.e., higher CSR) and longer loading periods (i.e., smaller *f*) resulted in greater degradation of the soil fabric, higher *EPWP* and increased axial strain at a lower number of cycles. The ε_t of compacted specimens was approximately 0.36%, which was lower than the consolidated specimens (0.47%). The *EPWP* build-up was notably higher in the compacted specimens due to the collapse of the large pores and the earlier fabric degradation (at a smaller ε_t). For example, the $EPWP/p'_0$ for compacted specimens reached 0.92 at ε_a = 10% but was less than 0.63 for the consolidated specimens. Previous studies (Dobry and Vucetic 1987; Vucetic 1994; Lei *et al.* 2016) suggested a threshold strain above which a rapid increase in *EPWP* and soil deformation would occur. In this study, it was found that such a threshold strain could change significantly with the initial soil fabric, i.e., the larger and less connected pores created by compaction experienced an earlier degradation in soil fabric, which triggered instability.

Figure 12 shows that N_c tends to increase linearly in the logarithmic scale as the specimens were subjected to higher frequencies and lower CSR. There is a bifurcation in the level of N_c that occurs at different loading frequencies, depending on the CSRs and the specimen fabric. For example, in specimens under CSR = 0.2 and frequency of 1 Hz, N_c was respectively 1512 and 1107 cycles for consolidated and compacted specimens; however, as the frequency increased to 5 Hz, N_c increased to 19775 cycles for the consolidated specimen, whereas only 4785 cycles (nearly one-fourth) were reached by the compacted specimen at the same frequency. More interestingly, an inverse trend was observed under CSR = 0.3. At a frequency 1 Hz, N_c was 48 and 12 cycles for the consolidated and compacted specimens, respectively, but as the frequency increased to 5 Hz, the N_c increased swiftly to 159 cycles for the compacted specimen, while a more moderate increase occurred for the consolidated specimen that reached N_c = 238 cycles. This behaviour can be explained by the fabric that is rearranged during cyclic loading; under a low CSR (e.g., 0.2), the soil fabric is gradually rearranged during loading and the effect of the loading frequency becomes more significant. The homogeneous and robust fabric of the consolidated specimens ensured that a greater number of cycles could be sustained before a significant deformation occurred, leading to a greater cyclic resistance. However, when the CSR increased to 0.3 the rate that the soil fabric degraded and the *EPWP* developed increased, which diminished the effect that the loading frequency had on the onset of soil instability. However, the compacted specimens experienced a greater influence of frequency because their open fabric with large pores was more vulnerable to sudden collapse, e.g., $N_c < 30$ for $f < 2$Hz.

Figure 13Figure 13 shows typical stress-strain plots for consolidated and compacted specimens subjected to cyclic loading at CSR = 0.2 – 0.3 and a frequency of 1 Hz. All the specimens experienced a reduction in the deviator stress with the development of axial strain (i.e., cyclic softening), which agrees with previous findings for fine-grained soils subjected to CSR > CSR_c (Zhou and Gong 2001; Indraratna *et al.* 2020b). Nevertheless, the compacted specimens exhibited a rapid loss in strength with higher axial strain per cycle. For example, in those specimens subjected to CSR = 0.3, the deviator stress in the compacted specimen dropped from 40 kPa to 33 kPa, but only 38 kPa in the consolidated specimen at ε_a = 1%. The stress paths for all consolidated and compacted specimens are shown in Figure 14. Since these specimens were subjected to cyclic loading the *EPWP* increased and the stress paths migrated to the left until they failed due to cyclic softening. The specimens prepared by compaction experienced a more significant drop in effective stress than those prepared by consolidation. This observation confirmed that compaction created a more unstable fabric which resulted in more cyclic degradation. The consolidated specimens seemed to fail when the stress paths reached the CSL defined from monotonic tests, whereas the stress path of the compacted specimen crossed the CSL. Previous studies showed contradicting results with regard to the relationship between the monotonic and cyclic response of soils. For example, Georgiannou *et al.* (1991) and Yang and Pan (2017) found that a monotonic response sets a boundary for cyclic failure, while Sakai *et al.* (2003) and Dzaklo *et al.* (2021) showed that the cyclic stress path can cross the CSL. However, none of them addressed the influence of soil fabric. This study shows that the soil fabric plays a key role in determining whether the parameters obtained from monotonic tests could be used to predict cyclic failure. Nevertheless, a detailed mathematical correlation between the fabric features of the soil and its shear behaviour could not be established due to the limited Micro-CT scanning data for pores < 11 μm.

4 Conclusion

This study has significantly advanced our understanding of the influence of soil fabric on the monotonic and cyclic shear responses of a subgrade soil through an extensive laboratory investigation. Following common field practice of rail track construction, two different specimen preparation methods, i.e., slurry consolidation and compaction, were used to create specimens having distinct soil fabrics, which were then subjected to a series of monotonic and cyclic shearing tests. Based on the findings of this study, the following conclusions can be drawn.

- The consolidation process resulted in a soil fabric with much smaller (d_{60} = 67.4 μm) and more interconnected pores compared to the compacted soil specimens (d_{60} = 129 μm). The number of pores per volume and the average specific surface area of the pores in the consolidated specimens were considerably greater than those in the compacted specimens. It could be concluded that the dynamic compaction process would form larger particle clusters allowing increased pore sizes within the compacted soil fabric.
- There was no evidence that the soil fabric influenced the values of C_c and C_s significantly. However, any change in the soil fabric would cause distinctive values of soil properties, for instance, in relation to the yield stress σ'_{vc} (i.e., 18kPa and 35 kPa for compacted and consolidated specimens, respectively) and the compressibility coefficient, c_v (115.2 m^2/year and 5.5 m^2/year for compacted and consolidated specimens, respectively). Interestingly, the compressibility of the compacted specimen became higher upon reaching σ'_{vc}. This can be attributed to the collapse

of the open soil fabric, thus leading to the conclusion that the compaction method contributes to a weaker soil fabric compared to the consolidation technique.

- The hydraulic measurement showed that the compacted specimen had a larger permeability than its counterpart by approximately two orders of magnitude; for example, at $e = 0.67$, $k_{\text{comp}} = 3.5 \cdot 10^{-7}$ and $k_{\text{cons}} = 4.1 \cdot 10^{-9}$ m/s. One may draw the conclusion that this observation is attributed to the creation of much larger pores with a lower specific surface area in the compacted soil compared to the slurry consolidation technique.
- During isotropic shearing, the consolidated specimens exhibited an elastic-perfectly plastic behaviour, while the compacted specimens experienced a phase transformation, whereby the contractive soil behaviour changed to a dilative nature. During anisotropic shearing, compacted specimens with larger and less interconnected pores showed greater strain softening and larger development of *EPWP* regardless of the stress ratio, *K*. This corresponded to a much lower residual shear strength (e.g., for $K = 0.5$, $q_{res} \cong 26$ kPa and 20 kPa for compacted and consolidated specimens), with only a marginal effect on the maximum deviator stress, q_{max}. These observations proved beyond doubt that the fabric of the soil would have a considerable influence on its stress-strain response, even though its critical state line seemed relatively unaffected by the transformed fabric.
- The effects of the cyclic stress ratio (CSR) and the frequency (f) on the shear behaviour changed considerably with the initial soil fabric and its subsequent degradation. When subjected to increasing values of CSR and f, the compacted specimens failed at a smaller number of cycles (N_c) due to an increasingly unstable fabric having larger particle clusters allowing larger pore sizes. In addition, the compacted specimens experienced a more significant build-up of *EPWP* during cyclic shearing corresponding to an earlier degradation at $\varepsilon_t = 0.36\%$ compared to $\varepsilon_t = 0.47\%$ for the consolidated specimens. This proved that a soil specimen formed by the consolidation method could resist deformation under cyclic loading better compared to a compacted counterpart.

- The test results showed that the cyclic stress paths of consolidated specimens were bounded by the corresponding critical state line (CSL) based on monotonic shearing, whereas the stress paths of the compacted specimens crossed over the monotonic CSL. Therefore, based on the results of this study, it is important to exercise caution if conventional critical state parameters obtained from static tests are used to predict failure under cyclic loading.

Acknowledgments

This research was supported by the Australian Government through the Australian Research Council's Linkage Projects funding scheme (LP160101254), and the Transport Research Centre (TRC), University of Technology Sydney. The financial and technical support from SMEC, Coffey, Australasian Centre for Rail Innovation (ACRI) and Sydney Trains are much appreciated. The micro-CT scanning was conducted at the SMART Infrastructure Facility at the University of Wollongong.

Competing interests

The authors declare there are no competing interests.

Author contribution statement

I.N.S.: Resources, methodology, investigation, formal analysis, validation, writing – original draft.

B.I.: Conceptualization, funding acquisition, project administration, supervision, writing review and editing.

T.T.N.: Conceptualization, methodology, supervision, formal analysis, writing review and editing.

C.R.: Funding acquisition, project administration, supervision, writing review and editing.

Data Availability

Data analysed during this study are provided in full within the published article.

References

ASTM C136/C136M-19. 2019. Standard test method for sieve analysis of fine and coarse aggregates. ASTM International, West Conshohocken, PA. doi: 10.1520/C0136_C0136M-19.

ASTM D698-12e2. 2012. Standard test methods for laboratory compaction characteristics of soil using standard effort (12 400 ft-lbf/ft3 (600 kN-m/m3)). ASTM International, West Conshohocken, PA. doi: 10.1520/D0698-12E02.

ASTM D854-14. 2014. Standard test methods for specific gravity of soil solids by water pycnometer. ASTM International, West Conshohocken, PA. doi: 10.1520/D0854-14.

ASTM D2435/D2435M-11. 2020. Standard test methods for one-dimensional consolidation properties of soils using incremental loading. ASTM International, West Conshohocken, PA. doi: 10.1520/D2435_D2435M-11R20.

ASTM D2487-17e1. 2017. Standard practice for classification of soils for engineering purposes (Unified Soil Classification System). ASTM International, West Conshohocken, PA. doi: 10.1520/D2487-17E01.

ASTM D4318-17e1. 2017. Standard test methods for liquid limit, plastic limit and plasticity index of soils. ASTM International, West Conshohocken, PA. doi: 10.1520/D4318-17E01.

Bayat, M., Bayat, E., Aminpour, H. and Salarpour, A. 2014. Shear strength and pore-water pressure characteristics of sandy soil mixed with plastic fine. Arabian Journal of Geosciences, **7**(3): 1049-1057. doi: 10.1007/s12517-012-0753-9.

Burghignoli, A., Miliziano, S. and Soccodato, F.M. 2010. Cementation effects in two lacustrine clayey soils. Geotechnical and Geological Engineering, **28**(6): 815-833. doi: 10.1007/s10706-010-9343-3.

Burland, J.B. 1990. On the compressibility and shear strength of natural clays. Géotechnique, **40**(3): 329-378. doi: 10.1680/geot.1990.40.3.329.

Burton, G.J., Pineda, J.A., Sheng, D. and Airey, D. 2015. Microstructural changes of an undisturbed, reconstituted and compacted high plasticity clay subjected to wetting and drying. Engineering Geology, **193**: 363-373. doi: 10.1016/j.enggeo.2015.05.010.

Cabalar, A.F. and Mustafa, W.S. 2017. Behaviour of sand–clay mixtures for road pavement subgrade. International Journal of Pavement Engineering, **18**(8): 714-726. doi: 10.1080/10298436.2015.1121782.

Cai, Y., Hao, B., Gu, C., Wang, J. and Pan, L. 2018. Effect of anisotropic consolidation stress paths on the undrained shear behavior of reconstituted Wenzhou Clay. Engineering Geology, **242**: 23-33. doi: 10.1016/j.enggeo.2018.05.016.

Chen, X., Qian, J., Zhang, L. and Ling, J. 2020. Investigating the Combined Effects of Inherent and Stress-Induced Anisotropy on the Mechanical Behavior of Granular Materials Using Three-Dimensional Discrete Element Method. Mathematical Problems in Engineering, **2020**: 7841824. doi: 10.1155/2020/7841824.

Chu, J., Indraratna, B., Yan, S. and Rujikiatkamjorn, C. 2014. Overview of preloading methods for soil improvement. Proceedings of the Institution of Civil Engineers - Ground Improvement, **167**(3): 173-185. doi: 10.1680/grim.13.00022.

Cnudde, V., Boone, M., Dewanckele, J., Dierick, M., van Hoorebeke, L. and Jacobs, P. 2011. 3D characterization of sandstone by means of X-ray computed tomography. Geosphere, **7**(1): 54-61. doi: 10.1130/GES00563.1.

Cnudde, V. and Boone, M.N. 2013. High-resolution X-ray computed tomography in geosciences: A review of the current technology and applications. Earth-Science Reviews, **123**: 1-17. doi: 10.1016/j.earscirev.2013.04.003.

Dobry, R. and Vucetic, M. 1987. Dynamic properties and seismic response of soft clay deposits. *In:* International Symposium on Geotechnical Engineering of Soft Soils. pp. 51-87.

Dzaklo, C.K., Rujikiatkamjorn, C., Indraratna, B. and Kelly, R. 2021. Cyclic behaviour of compacted black soil-coal wash matrix. Engineering Geology, **294**: 106385. doi: 10.1016/j.enggeo.2021.106385.

Fonseca, A.V.d., Rios, S. and Amaral, M.F. 2013a. Structural anisotropy by static compaction. Engineering Geology, **154**: 89-97. doi: 10.1016/j.enggeo.2012.11.012.

Fonseca, J., O'Sullivan, C., Coop, M.R. and Lee, P.D. 2013b. Quantifying the evolution of soil fabric during shearing using directional parameters. Géotechnique, **63**(6): 487-499. doi: 10.1680/geot.12.P.003.

Fonseca, J., O'Sullivan, C., Coop, M.R. and Lee, P.D. 2013c. Quantifying the evolution of soil fabric during shearing using scalar parameters. Géotechnique, **63**(10): 818-829. doi: 10.1680/geot.11.P.150.

Gasparre, A., Nishimura, S., Coop, M.R. and Jardine, R.J. 2007. The influence of structure on the behaviour of London Clay. Géotechnique, **57**(1): 19-31. doi: 10.1680/geot.2007.57.1.19.

Ge, M., Pineda, J.A., Sheng, D., Burton, G.J. and Li, N. 2021. Microstructural effects on the wetting-induced collapse in compacted loess. Computers and Geotechnics, **138**: 104359. doi: 10.1016/j.compgeo.2021.104359.

Georgiannou, V., Hight, D. and Burland, J. 1991. Behaviour of clayey sands under undrained cyclic triaxial loading. Géotechnique, **41**(3): 383-393. doi: 10.1680/geot.1991.41.3.383.

Georgiannou, V.N., Konstadinou, M. and Triantafyllos, P. 2018. Sand Behavior under Stress States Involving Principal Stress Rotation. Journal of Geotechnical and Geoenvironmental Engineering, **144**(6): 04018028. doi: 10.1061/(ASCE)GT.1943-5606.0001878.

Gonzalez, R.C. and Woods, R.E. 2018. Digital Image Processing. Pearson Education, England.

Hussaini, S.R. and Dvorkin, J. 2021. Specific surface area versus porosity from digital images. Journal of Petroleum Science and Engineering, **196**: 107773. doi: 10.1016/j.petrol.2020.107773.

Hyde, A.F.L., Higuchi, T. and Yasuhara, K. 2006. Liquefaction, cyclic mobility, and failure of silt. Journal of Geotechnical and Geoenvironmental Engineering, **132**(6): 716-735. doi: 10.1061/(ASCE)1090-0241(2006)132:6(716).

Hyodo, M., Yamamoto, Y. and Sugiyama, M. 1994. Undrained Cyclic Shear Behaviour of Normally Consolidated Clay Subjected to Initial Static Shear Stress. Soils and Foundations, **34**(4): 1-11. doi: 10.3208/sandf1972.34.4_1.

Indraratna, B., Baral, P., Rujikiatkamjorn, C. and Perera, D. 2018. Class A and C predictions for Ballina trial embankment with vertical drains using standard test data from industry and large diameter test specimens. Computers and Geotechnics, **93**: 232-246. doi: 10.1016/j.compgeo.2017.06.013.

Indraratna, B., Korkitsuntornsan, W. and Nguyen, T.T. 2020a. Influence of Kaolin content on the cyclic loading response of railway subgrade. Transportation Geotechnics, **22**: 100319. doi: 10.1016/j.trgeo.2020.100319.

Indraratna, B., Nimbalkar, S., Christie, D., Rujikiatkamjorn, C. and Vinod, J. 2010. Field Assessment of the Performance of a Ballasted Rail Track with and without Geosynthetics. Journal of Geotechnical and Geoenvironmental Engineering, **136**(7): 907-917. doi: doi:10.1061/(ASCE)GT.1943-5606.0000312.

Indraratna, B., Singh, M., Nguyen, T.T., Leroueil, S., Abeywickrama, A., Kelly, R. and Neville, T. 2020b. A laboratory study on fluidization of subgrade under undrained cyclic triaxial tests. Canadian Geotechnical Journal, **57**(11): 1767-1779. doi: 10.1139/cgj-2019-0350.

Jana, A. and Stuedlein, A.W. 2021. Monotonic, Cyclic, and Postcyclic Responses of an Alluvial Plastic Silt Deposit. Journal of Geotechnical and Geoenvironmental Engineering, **147**(3): 04020174. doi: 10.1061/(ASCE)GT.1943-5606.0002462.

Jotisankasa, A., Coop, M. and Ridley, A. 2009. The mechanical behaviour of an unsaturated compacted silty clay. Géotechnique, **59**(5): 415-428. doi: 10.1680/geot.2007.00060.

Jung, Y.-H., Finno, R.J. and Cho, W. 2012. Stress-strain responses of reconstituted and natural compressible Chicago glacial clay. Engineering Geology, **129-130**: 9-19. doi: 10.1016/j.enggeo.2012.01.003.

Lei, H., Li, B., Lu, H. and Ren, Q. 2016. Dynamic Deformation Behavior and Cyclic Degradation of Ultrasoft Soil under Cyclic Loading. Journal of Materials in Civil Engineering, **28**(11): 04016135. doi: 10.1061/(ASCE)MT.1943-5533.0001641.

Leroueil, S. and Vaughan, P.R. 1990. The general and congruent effects of structure in natural soils and weak rocks. Géotechnique, **40**(3): 467-488. doi: 10.1680/geot.1990.40.3.467.

Li, L., Zhong, R. and Nimbalkar, S. 2018. Finite element model of ballasted railway with infinite boundaries considering effects of moving train loads and Rayleigh waves. Soil Dynamics and Earthquake Engineering, **114**: 147-153. doi: 10.1016/j.soildyn.2018.06.033.

Li, X. and Li, X.-S. 2009. Micro-Macro Quantification of the Internal Structure of Granular Materials. Journal of Engineering Mechanics, **135**(7): 641-656. doi: 10.1061/(ASCE)0733-9399(2009)135:7(641).

Liu, J. and Xiao, J. 2010. Experimental Study on the Stability of Railroad Silt Subgrade with Increasing Train Speed. Journal of Geotechnical and Geoenvironmental Engineering, **136**(6): 833-841. doi: 10.1061/(ASCE)GT.1943-5606.0000282.

Liu, M.D. and Carter, J.P. 2002. A structured Cam Clay model. Canadian Geotechnical Journal, **39**(6): 1313-1332. doi: 10.1139/t02-069.

Mamou, A., Powrie, W., Priest, J.A. and Clayton, C. 2017. The effects of drainage on the behaviour of railway track foundation materials during cyclic loading. Géotechnique, **67**(10): 845-854. doi: 10.1680/jgeot.15.P.278.

MathWorks. 2019. MATLAB release R2019B, version 9.7.0. The MatWorks Inc., Natick, Massachusetts, USA.

Mavko, G., Mukerji, T. and Dvorkin, J. 2009. The rock physics handbook: tools for seismic analysis of porous media. Cambridge University Press, New York, NY.

Mitchell, J.K. and Soga, K. 2005. Fundamentals of soil behavior. John Wiley & Sons, Hoboken, New Jersey.

Nguyen, C.D., Benahmed, N., Andò, E., Sibille, L. and Philippe, P. 2019. Experimental investigation of microstructural changes in soils eroded by suffusion using X-ray tomography. Acta Geotechnica, **14**: 749-765. doi: 10.1007/s11440-019-00787-w.

Nguyen, T.T. and Indraratna, B. 2019. Micro-CT Scanning to Examine Soil Clogging Behavior of Natural Fiber Drains. Journal of Geotechnical and Geoenvironmental Engineering, **145**(9): 04019037. doi: 10.1061/(ASCE)GT.1943-5606.0002065.

Otsu, N. 1979. A Threshold Selection Method from Gray-Level Histograms. IEEE Transactions on Systems, Man, and Cybernetics, **9**(1): 62-66. doi: 10.1109/TSMC.1979.4310076.

Pan, K., Yang, Z.X. and Xu, T.T. 2018. Impact of Static Preshearing on Undrained Anisotropy and Shear Characteristics of Sand. International Journal of Geomechanics, **18**(12): 04018162. doi: 10.1061/(ASCE)GM.1943-5622.0001319.

Pillai, R.J., Robinson, R.G. and Boominathan, A. 2011. Effect of Microfabric on Undrained Static and Cyclic Behavior of Kaolin Clay. Journal of Geotechnical and Geoenvironmental Engineering, **137**(4): 421-429. doi: 10.1061/(ASCE)GT.1943-5606.0000442.

Pineda, J.A., Suwal, L.P., Kelly, R.B., Bates, L. and Sloan, S.W. 2016. Characterisation of Ballina clay. Géotechnique, **66**(7): 556-577. doi: 10.1680/jgeot.15.P.181.

Prakasha, K.S. and Chandrasekaran, V.S. 2005. Behavior of Marine Sand-Clay Mixtures under Static and Cyclic Triaxial Shear. Journal of Geotechnical and Geoenvironmental Engineering, **131**(2): 213-222. doi: doi:10.1061/(ASCE)1090-0241(2005)131:2(213).

Priest, J.A., Powrie, W., Yang, L., Grabe, P.J. and Clayton, C.R.I. 2010. Measurements of transient ground movements below a ballasted railway line. Géotechnique, **60**(9): 667-677. doi: 10.1680/geot.7.00172.

Rabbani, A., Ayatollahi, S., Kharrat, R. and Dashti, N. 2016. Estimation of 3-D pore network coordination number of rocks from watershed segmentation of a single 2-D image. Advances in Water Resources, **94**: 264-277. doi: 10.1016/j.advwatres.2016.05.020.

Rabbani, A., Jamshidi, S. and Salehi, S. 2014. An automated simple algorithm for realistic pore network extraction from micro-tomography images. Journal of Petroleum Science and Engineering, **123**: 164-171. doi: 10.1016/j.petrol.2014.08.020.

Ren, L., Ghani, M.U., Wu, D., Zheng, B., Chen, Y., Yang, K., Wu, X. and Liu, H. 2016. The impact of spectral filtration on image quality in micro-CT system. Journal of Applied Clinical Medical Physics, **17**(1): 301-315. doi: 10.1120/jacmp.v17i1.5714.

Romero, E. 2013. A microstructural insight into compacted clayey soils and their hydraulic properties. Engineering Geology, **165**: 3-19. doi: 10.1016/j.enggeo.2013.05.024.

Sakai, A., Samang, L. and Miura, N. 2003. Partially-Drained Cyclic Behavior and its Application to the Settlement of a low Embankment Road on Silty-Clay. Soils and Foundations, **43**(1): 33-46. doi: 10.3208/sandf.43.33.

Shi, Y. and Yan, W.M. 2015. Segmentation of irregular porous particles of various sizes from X-ray microfocus computer tomography images using a novel adaptive watershed approach. Géotechnique Letters, **5**(4): 299-305. doi: 10.1680/jgele.15.00100.

Silva, I.N., Indraratna, B., Nguyen, T.T. and Rujikiatkamjorn, C. 2022. Shear behaviour of subgrade soil with reference to varying initial shear stress and plasticity index. Acta Geotechnica, **17**: 4207-4216. doi: 10.1007/s11440-022-01477-w.

Sivakumar, V., Doran, I.G. and Graham, J. 2002. Particle orientation and its influence on the mechanical behaviour of isotropically consolidated reconstituted clay. Engineering Geology, **66**(3-4): 197-209. doi: 10.1016/S0013-7952(02)00040-6.

SkyScan NV. 2011. NRecon user manual. Bruker microCT, Kontich, Belgium.

Sze, H.Y. and Yang, J. 2014. Failure Modes of Sand in Undrained Cyclic Loading: Impact of Sample Preparation. Journal of Geotechnical and Geoenvironmental Engineering, **140**(1): 152-169. doi: 10.1061/(ASCE)GT.1943-5606.0000971.

Tarantino, A. 2011. Unsaturated soils: Compacted versus reconstituted states. *In:* 5th International Conference on Unsaturated Soils. pp. 113-136.

Taylor, H.F., O'Sullivan, C. and Sim, W.W. 2015. A new method to identify void constrictions in micro-CT images of sand. Computers and Geotechnics, **69**: 279-290. doi: 10.1016/j.compgeo.2015.05.012.

Trinh, V.N., Tang, A.M., Cui, Y.J., Dupla, J.C., Canou, J., Calon, N., Lambert, L., Robinet, A. and Schoen, O. 2012. Mechanical characterisation of the fouled ballast in ancient railway track substructure by large-scale triaxial tests. Soils and Foundations, **52**(3): 511-523. doi: 10.1016/j.sandf.2012.05.009.

Vaid, Y.P. and Sivathayalan, S. 2000. Fundamental factors affecting liquefaction susceptibility of sands. Canadian Geotechnical Journal, **37**(3): 592-606. doi: 10.1139/t00-040.

Vucetic, M. 1994. Cyclic Threshold Shear Strains in Soils. Journal of Geotechnical Engineering, **120**(12): 2208-2228. doi: 10.1061/(ASCE)0733-9410(1994)120:12(2208).

Wichtmann, T., Steller, K. and Triantafyllidis, T. 2020. On the influence of the sample preparation method on strain accumulation in sand under high-cyclic loading. Soil Dynamics and Earthquake Engineering, **131**: 106028. doi: 10.1016/j.soildyn.2019.106028.

Wildenschild, D. and Sheppard, A.P. 2013. X-ray imaging and analysis techniques for quantifying pore-scale structure and processes in subsurface porous medium systems. Advances in Water Resources, **51**: 217-246. doi: 10.1016/j.advwatres.2012.07.018.

Yang, Z.X. and Pan, K. 2017. Flow deformation and cyclic resistance of saturated loose sand considering initial static shear effect. Soil Dynamics and Earthquake Engineering, **92**: 68-78. doi: 10.1016/j.soildyn.2016.09.002.

Yimsiri, S. and Soga, K. 2011. Effects of soil fabric on behaviors of granular soils: Microscopic modeling. Computers and Geotechnics, **38**(7): 861-874. doi: 10.1016/j.compgeo.2011.06.006.

Zhao, H.Y., Indraratna, B. and Ngo, T. 2021. Numerical simulation of the effect of moving loads on saturated subgrade soil. Computers and Geotechnics, **131**: 103930. doi: 10.1016/j.compgeo.2020.103930.

Zhou, J. and Gong, X. 2001. Strain degradation of saturated clay under cyclic loading. Canadian Geotechnical Journal, **38**(1): 208-212. doi: 10.1139/t00-062.

List of notations

C_c	Compression index
C_s	Swelling index
CSR	Cyclic stress ratio
c_v	Coefficient of consolidation
EPWP	Excess pore water pressure
f	Loading frequency
k	Coefficient of permeability
K	Ratio between horizontal and vertical stresses
K_0	Coefficient of earth pressure at rest
M	Slope of the critical state line
N	Number of cycles
N_c	Critical number of cycles
p'_0	Effective mean stress before shearing
q_{max}	Peak shear strength
q_{res}	Residual shear strength
ε_a	Axial strain
ε_t	Threshold axial strain
σ'_v	Effective vertical stress
$\bar{\sigma}'_v$	Average effective vertical stress
σ'_{vc}	Effective vertical pre-consolidation stress

Table 1: Summary of monotonic triaxial tests.

Specimen preparation method	Test no.	Initial properties			Consolidation stresses			After consolidation	
		w (%)	γ_d (kN/m^3)	e_0	σ'_3 (kPa)	σ'_1 (kPa)	K	γ_d (kN/m^3)	e
Consolidation	1	23.1	15.8	0.68	50	50	1.00	16.7	0.60
	2	23.6	15.9	0.67	75	75	1.00	17.1	0.56
	3	23.6	15.9	0.68	100	100	1.00	17.3	0.54
	4	23.9	15.9	0.67	150	150	1.00	17.7	0.51
	5	23.0	16.0	0.67	300	300	1.00	18.2	0.46
	6	22.7	16.0	0.67	25	50	0.50	16.4	0.62
	7	22.5	16.1	0.65	30	43	0.70	16.5	0.61
	8	22.8	16.2	0.65	34	36	0.94	16.7	0.60
Compaction	9	11.8	16.0	0.66	50	50	1.00	17.1	0.55
	10	11.3	16.0	0.66	75	75	1.00	17.5	0.52
	11	11.2	16.1	0.65	100	100	1.00	17.9	0.49
	12	11.7	16.1	0.66	150	150	1.00	18.2	0.46
	13	11.8	16.1	0.66	300	300	1.00	18.9	0.41
	14	11.5	16.0	0.66	25	50	0.50	16.9	0.58
	15	11.6	16.1	0.66	30	43	0.70	16.6	0.60
	16	11.8	16.0	0.66	34	36	0.94	16.5	0.62

Note: w = water content; γ_d = dry density; e = void ratio; σ'_3 effective confining pressure; σ'_1 effective axial stress;

K = ratio between effective horizontal and vertical stresses

Table 2: Summary of cyclic triaxial tests.

Specimen preparation method	Test no.	Initial properties			After consolidation		Cyclic loading parameters	
		w (%)	γ_d (kN/m³)	e_0	γ_d (kN/m³)	e	CSR	f (Hz)
Consolidation	1	21.6	16.4	0.64	16.6	0.60	0.2	1
	2	22.9	16.2	0.64	16.6	0.61		2
	3	21.9	16.2	0.65	16.5	0.61		3
	4	21.7	16.3	0.63	16.6	0.60		5
	5	23.1	15.9	0.68	16.3	0.64	0.3	1
	6	22.8	16.0	0.66	16.4	0.62		2
	7	21.9	16.0	0.66	16.4	0.62		3
	8	22.8	16.1	0.66	16.4	0.62		5
Compaction	9	11.6	16.0	0.66	16.6	0.61	0.2	1
	10	11.7	16.0	0.66	16.6	0.60		2
	11	11.4	16.0	0.66	16.7	0.60		3
	12	11.7	16.1	0.66	16.6	0.61		5
	13	11.4	16.2	0.65	16.8	0.59	0.3	1
	14	11.7	16.0	0.66	16.4	0.62		2
	15	11.5	16.0	0.66	16.6	0.61		3
	16	11.5	16.0	0.66	16.6	0.60		5

Note: w = water content; γ_d = dry density; e = void ratio; CSR cyclic stress ratio; f frequency

Figure captions

Figure 1: Samples prepared for triaxial testing by (a) consolidation and (b) compaction methods.

Figure 2: Summary of experimental procedures for triaxial shear tests.

Figure 3: Image processing of representative micro-CT scans of consolidated and compacted specimens: (a) – (b) selected ROIs; (c) – (d) binary ROIs.

Figure 4: Pore space characterisation: (a) pore size distribution (b) pore axis length distribution (c) circularity distribution of pores with Area > 100 pixels.

Figure 5: 3D reconstruction of VOIs: (a) – (b) solid and pore spaces (c) – (d) extracted pore spaces.

Figure 6: Pore Networks – Pore diameters and pore throats for (a) consolidated and (b) compacted specimens.

Figure 7: Consolidation tests on compacted and consolidated specimens: (a) compressibility curves (b) coefficient of consolidation c_v with $\overline{\sigma}'_v$ and (c) permeability at different void ratios.

Figure 8: Critical state surfaces of consolidated and compacted soils under isotropic undrained shear: (a) 3-dimensional scale and (b) projection on $p' - q$ (c) projection on p' (log scale) – v.

Figure 9: Isotropic shear responses of consolidated and compacted soils: (a) stress-strain curves (b) development of *EPWP* with axial strain.

Figure 10: Anisotropic shear responses of consolidated and compacted soils: (a) stress path (b) stress-strain curves (c) development of $EPWP/p'_0$ with axial strain and (d) shear strength at different values of *K*.

Figure 11: Development of ε_a and $EPWP/p'_0$ with the number of cycles for (a) consolidated and (b) compacted specimens.

Figure 12: Critical N_c trend at various *f* and *CSR*.

Figure 13: Typical stress-strain curves of soil specimens prepared by (a) consolidation and (b) compaction subjected to 1Hz.

Figure 14: Stress paths of specimens prepared by (a) consolidation and (b) compaction during cyclic shearing.

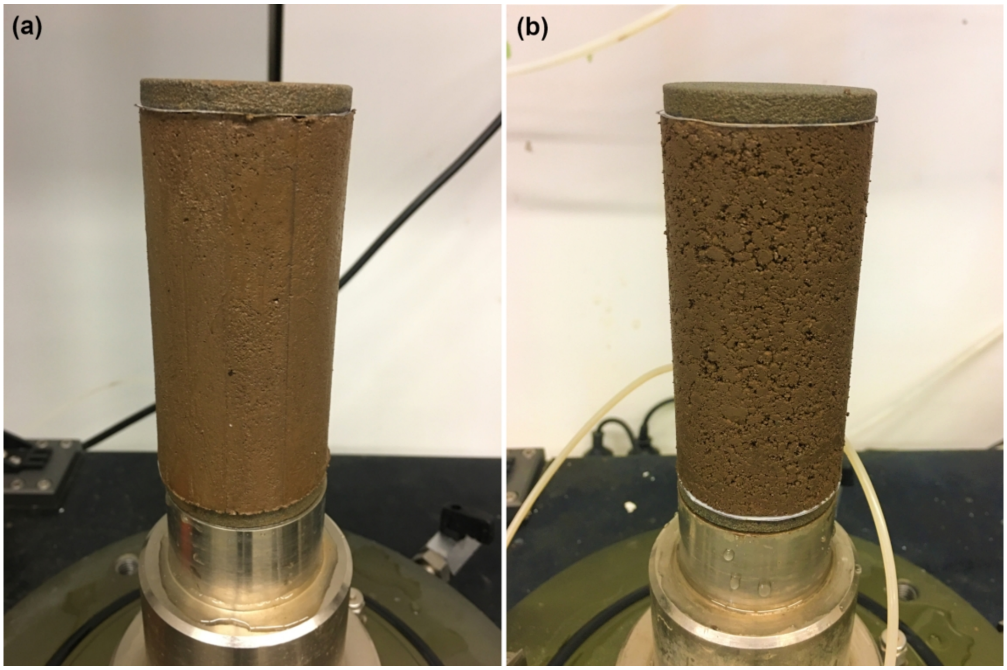

Figure 1: Samples prepared for triaxial testing by (a) consolidation and (b) compaction methods.

178x118mm (300 x 300 DPI)

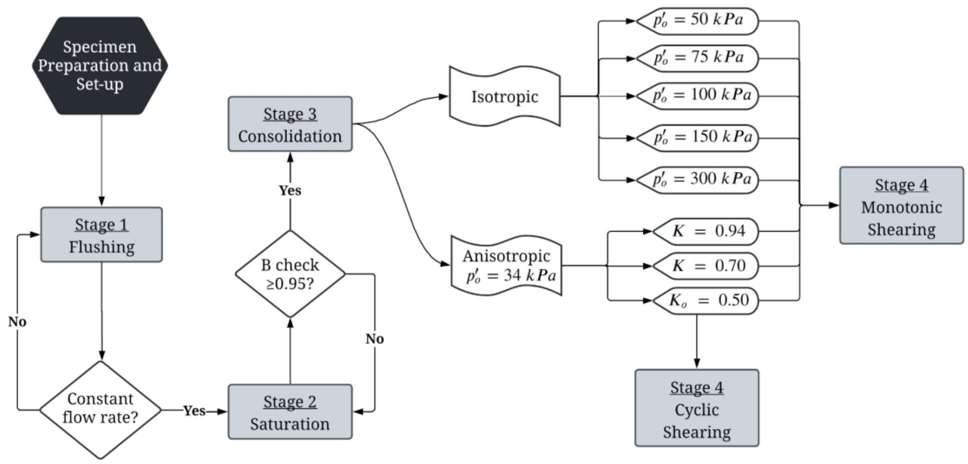

Figure 2: Summary of experimental procedures for triaxial shear tests.

181x89mm (300 x 300 DPI)

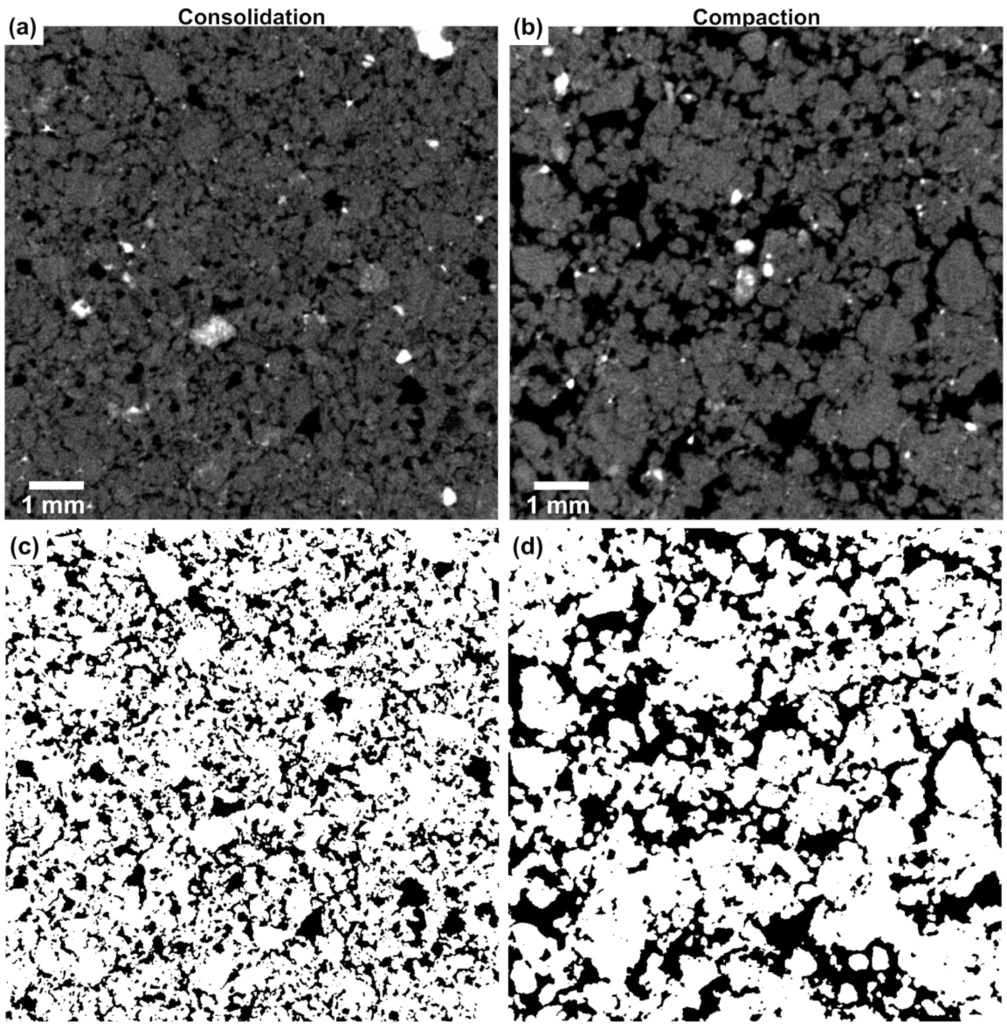

Figure 3: Image processing of representative micro-CT scans of consolidated and compacted specimens: (a) – (b) selected ROIs; (c) – (d) binary ROIs.

180x182mm (300 x 300 DPI)

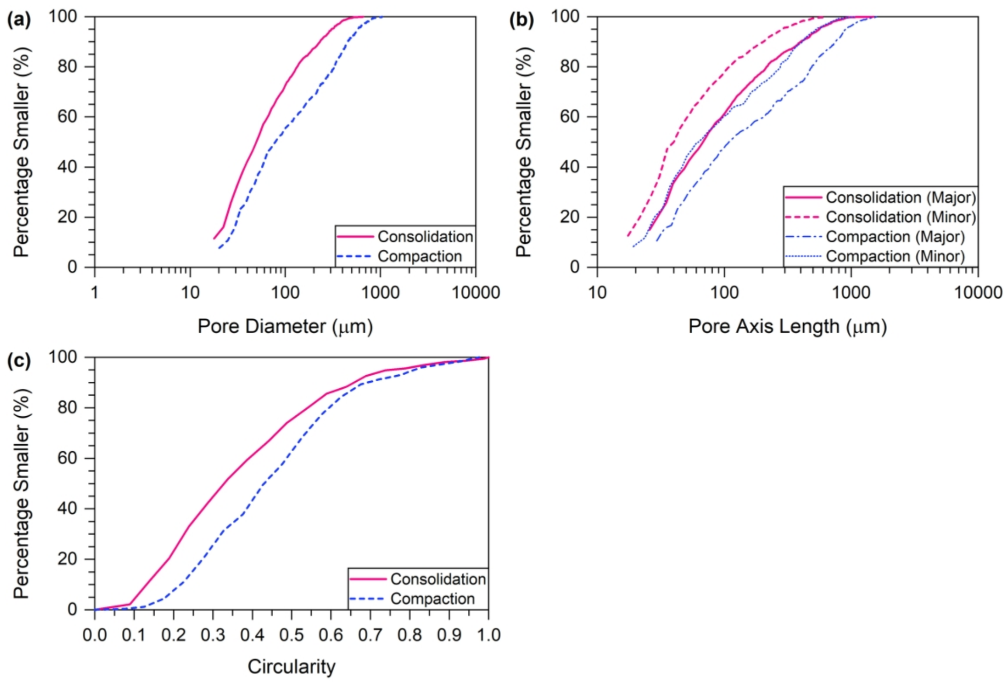

Figure 4: Pore space characterisation: (a) pore size distribution (b) pore axis length distribution (c) circularity distribution of pores with Area > 100 pixels.

178x121mm (300 x 300 DPI)

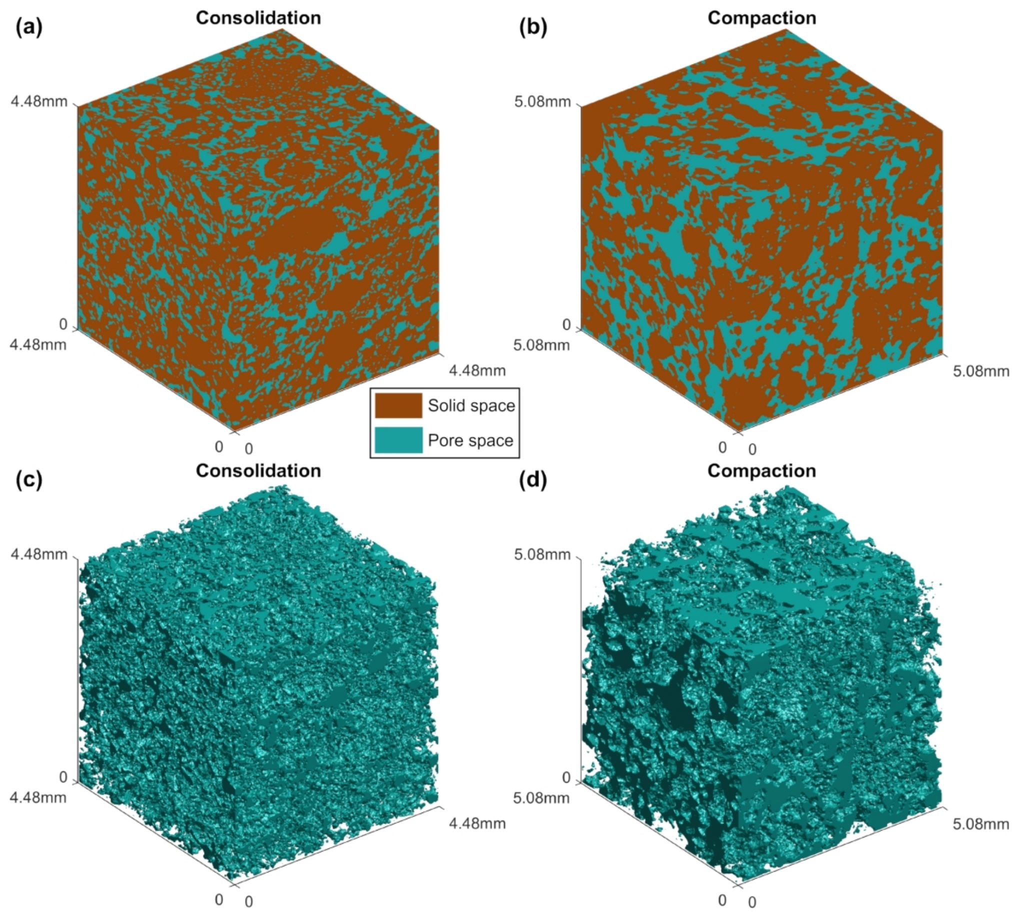

Figure 5: 3D reconstruction of VOIs: (a) – (b) solid and pore spaces (c) – (d) extracted pore spaces.

179x161mm (300 x 300 DPI)

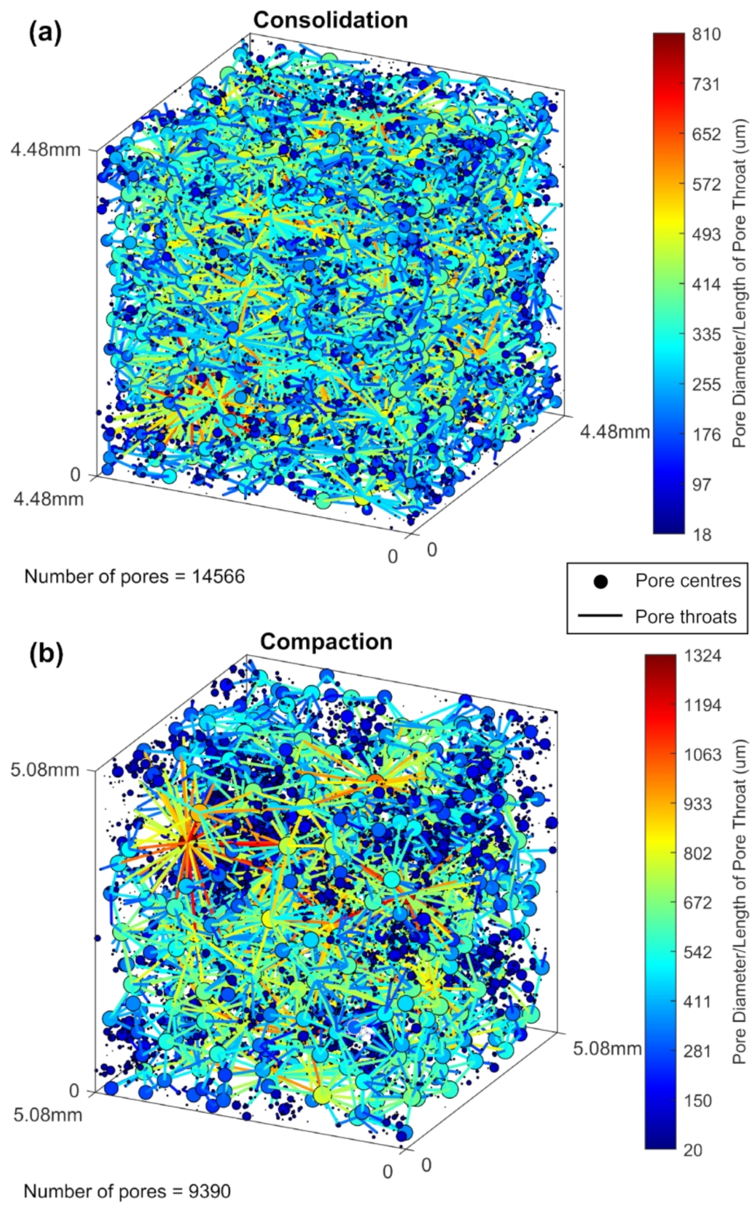

Figure 6: Pore Networks – Pore diameters and pore throats for (a) consolidated and (b) compacted specimens.

120x194mm (300 x 300 DPI)

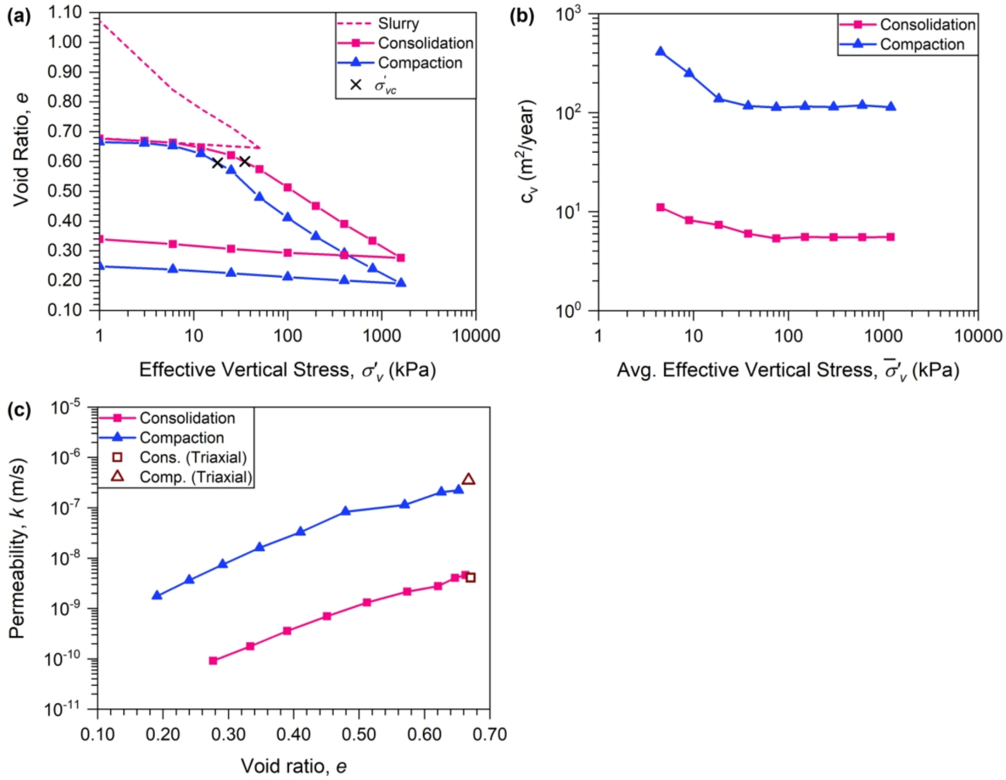

Figure 7: Consolidation tests on compacted and consolidated specimens: (a) compressibility curves (b) coefficient of consolidation cv with σ'$_v$ and (c) permeability at different void ratios.

178x139mm (300 x 300 DPI)

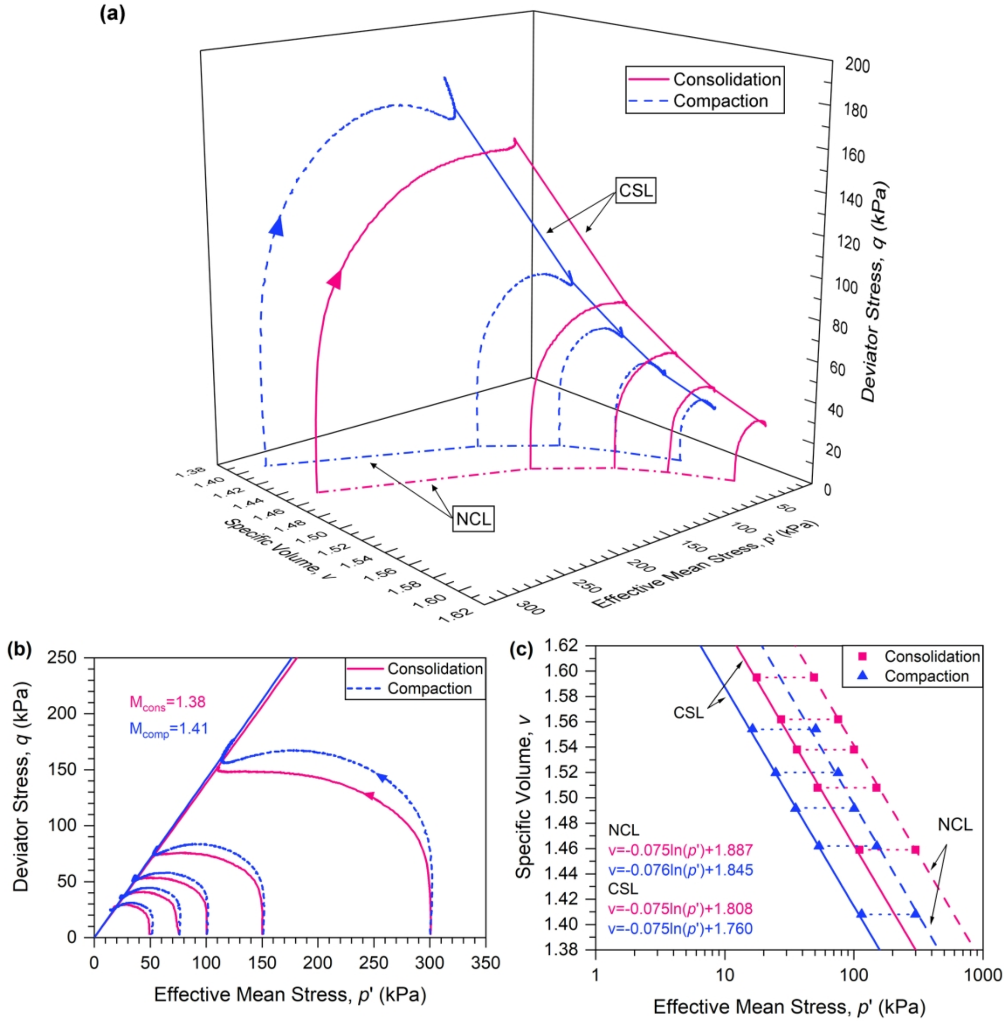

Figure 8: Critical state surfaces of consolidated and compacted soils under isotropic undrained shear: (a) 3-dimensional scale and (b) projection on p' – q (c) projection on p' (log scale) – v.

178x183mm (300 x 300 DPI)

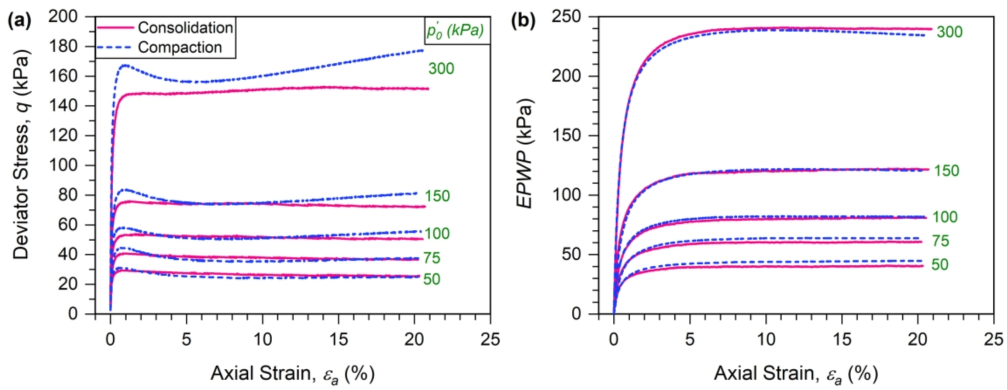

Figure 9: Isotropic shear responses of consolidated and compacted soils: (a) stress-strain curves (b) development of EPWP with axial strain.

178x69mm (300 x 300 DPI)

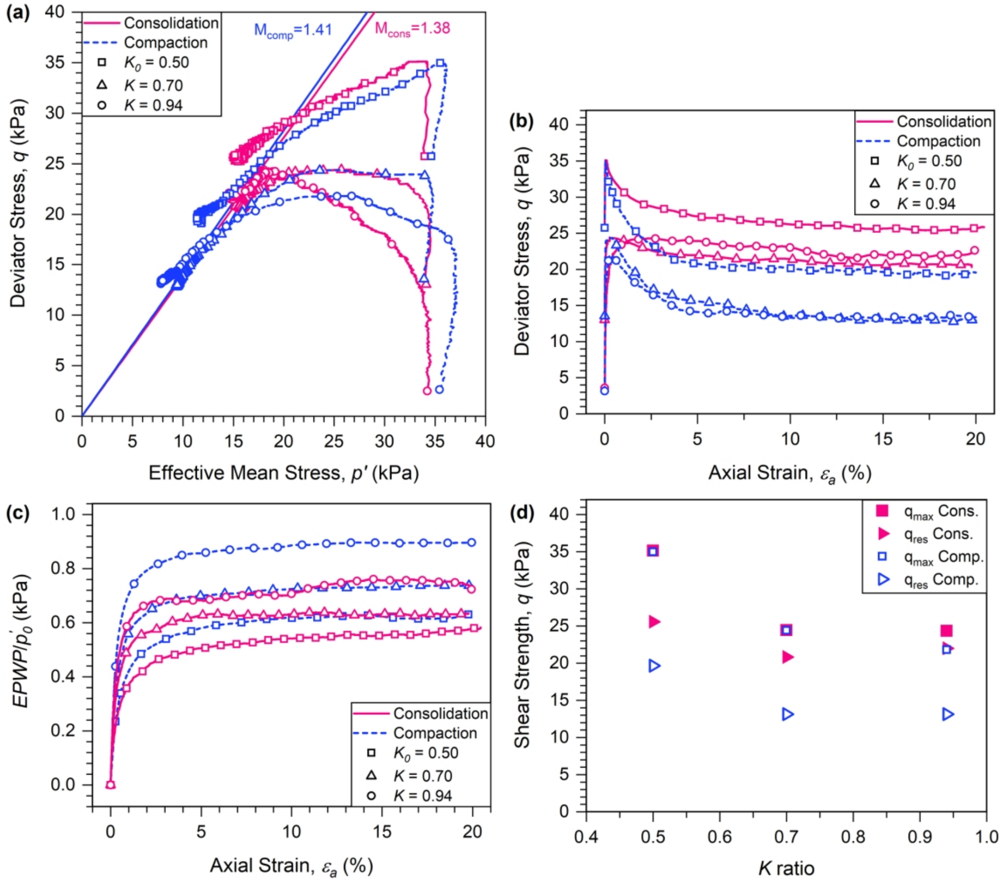

Figure 10: Anisotropic shear responses of consolidated and compacted soils: (a) stress path (b) stress-strain curves (c) development of EPWP/p_0' with axial strain and (d) shear strength at different values of K.

179x159mm (300 x 300 DPI)

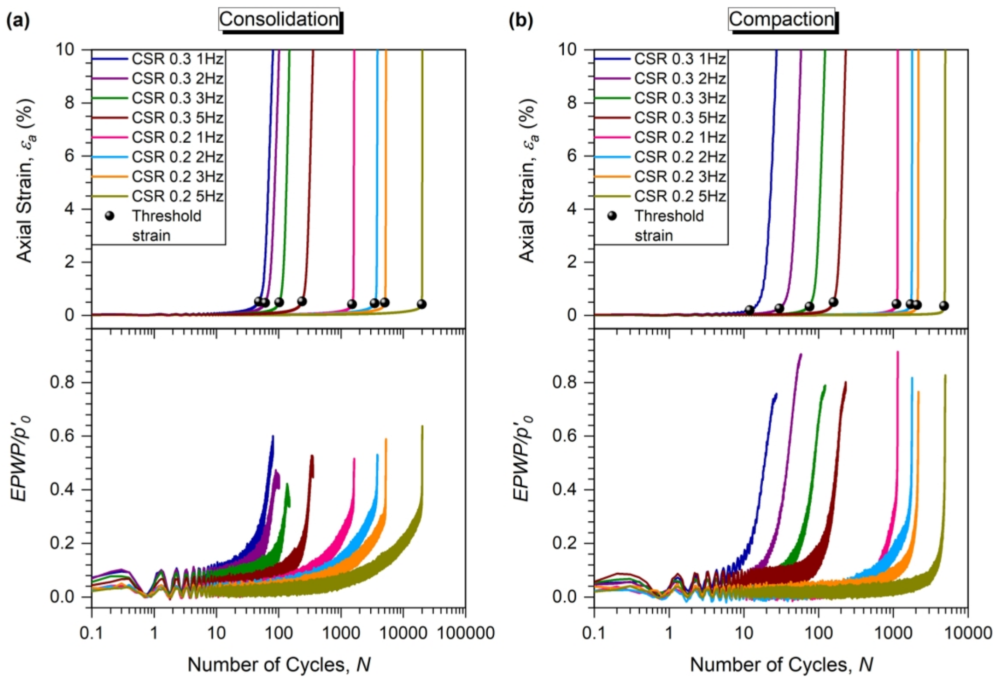

Figure 11: Development of ε_a and EPWP/p_0' with the number of cycles for (a) consolidated and (b) compacted specimens.

179x119mm (300 x 300 DPI)

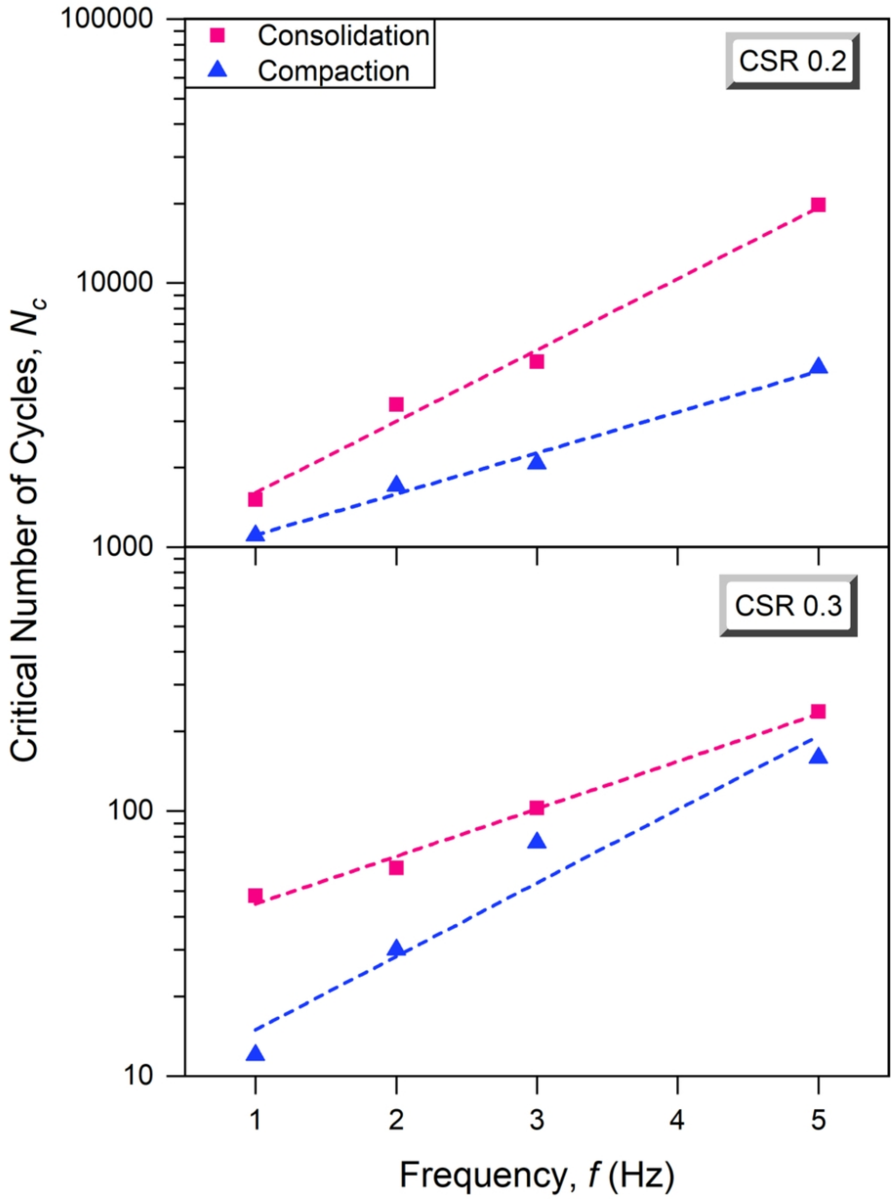

Figure 12: Critical Nc trend at various f and CSR.

88x118mm (300 x 300 DPI)

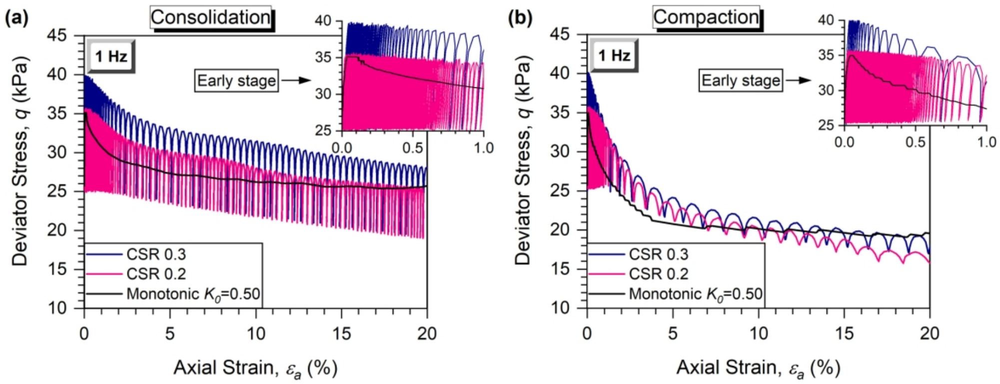

Figure 13: Typical stress-strain curves of soil specimens prepared by (a) consolidation and (b) compaction subjected to 1Hz.

178x69mm (300 x 300 DPI)

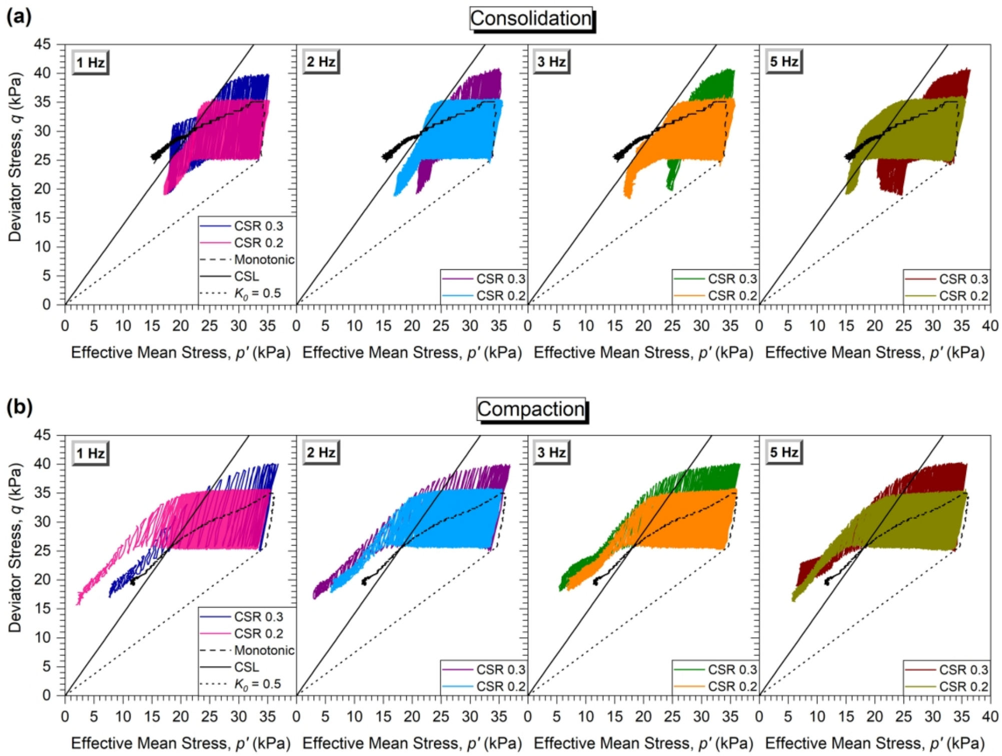

Figure 14: Stress paths of specimens prepared by (a) consolidation and (b) compaction during cyclic shearing.

181x141mm (300 x 300 DPI)